Li, Y., et al., 2023, Transient tin mineralization from cooling of magmatic fluids in a long-lived system: Geology, https://doi.org/10.1130/G50781.1

Transient tin mineralization from cooling of magmatic fluids in a long-lived system

Yang Li[1*], Jun-Yi Pan[2], Li-Guang Wu[3], Sheng He[3,4], Olivier Bachmann[5] and Xian-Hua Li[3]

[1]Ministry of Education Key Laboratory of Orogenic Belts and Crustal Evolution, School of Earth and Space Sciences, Peking University, Beijing 100871, China

[2]State Key Laboratory for Mineral Deposits Research, Department of Earth Sciences and Engineering, Nanjing University, Nanjing 210023, Jiangsu, China

[3]State Key Laboratory of Lithospheric Evolution, Institute of Geology and Geophysics, Chinese Academy of Sciences, Beijing 100029, China

[4]Beijing Research Institute of Uranium Geology, Beijing 100029, China

[5]Institute of Geochemistry and Petrology, Department of Earth Sciences, ETH Zurich, Zurich 8092, Switzerland

[*]Corresponding author, geoliy@outlook.com

1. Deposit geology and sample information

The Weilasituo Sn-polymetallic deposit is located in the eastern part of the Central Asian orogenic belt, which is a tin-polymetallic mineralization district with rapid increasing of tin reserves over the recent years (Mao et al., 2020). A series of granite-related polymetallic deposits were discovered in this area (Fig. S1), including the Huanggang Sn-Fe deposit, the Dajing Cu-Ag-Sn deposit, the Anle Sn-Ag-W deposit, the Bairendaba Ag-Pb-Zn deposit and the Weilasituo Sn-polymetallic deposits. Main strata in the area includes the Paleoproterozoic Baoyintu Group biotite plagioclase gneiss, the Carboniferous clastic rocks, carbonates, and felsic volcanics, and the Permian conglomerate, sandstone and shale. Intrusive rocks are widely distributed in this area, including Hercynian granite and quartz diorite, Yanshanian felsic volcanic rocks and granitoids. Most polymetallic deposits in this area are genetically linked to the Yanshanian magmatism (Mao et al., 2020).

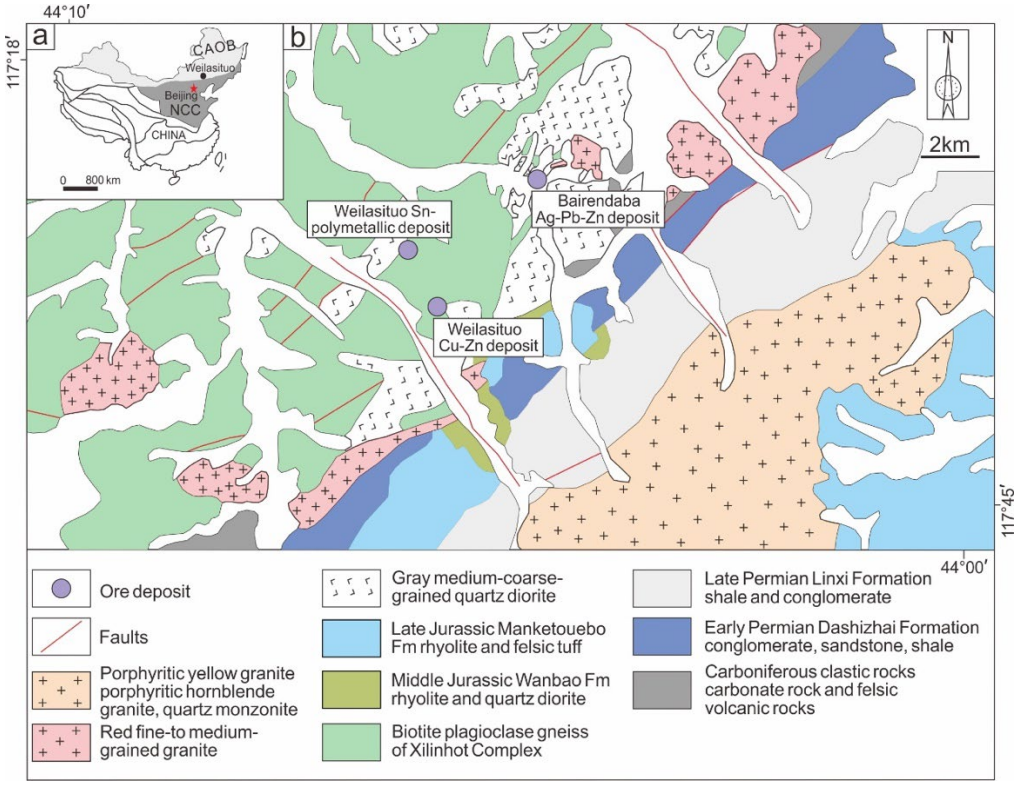

Figure S1. (a) Location of the Weilasituo Sn-polymetallic deposit. Abbreviation: CAOB: Central Asian Orogenic Belt; NCC: North China Craton. (b) Regional geological map of the Weilasituo and Bairendaba ore district, showing the distribution of granites, strata, structures and deposits (modified after Wang et al., 2017).

The Weilasituo Sn-polymetallic deposit has a proven reserve of >87,800 tons of Sn with an average grade of 1.2 %, >357,200 tons of Li_2O with an average grade of 1.3 %, 12,700 tons of WO_3 with an average grade of 0.2 %, 39,200 tons of Zn with an average grade of 2.6 % and 6,000 tons of Pb with an average grade of 0.6 %. Another two deposits, namely the Bairendaba Ag-Pb-Zn deposit and the Weilasituo Cu-Zn deposit all having much larger reserves of base metals, are spatially associated with the Weilasituo Sn-polymetallic deposit, but these two deposits contain no Sn. The main stratum in the mining area is the Paleoproterozoic Baoyintu Group, which is mainly composed of biotite plagioclase gneiss and hornblende plagioclase gneiss. The biotite plagioclase gneiss is the principal ore-hosting unit. The intrusive rocks in the area include quartz diorite and quartz porphyry, which are overlaid by an explosive breccia pipe.

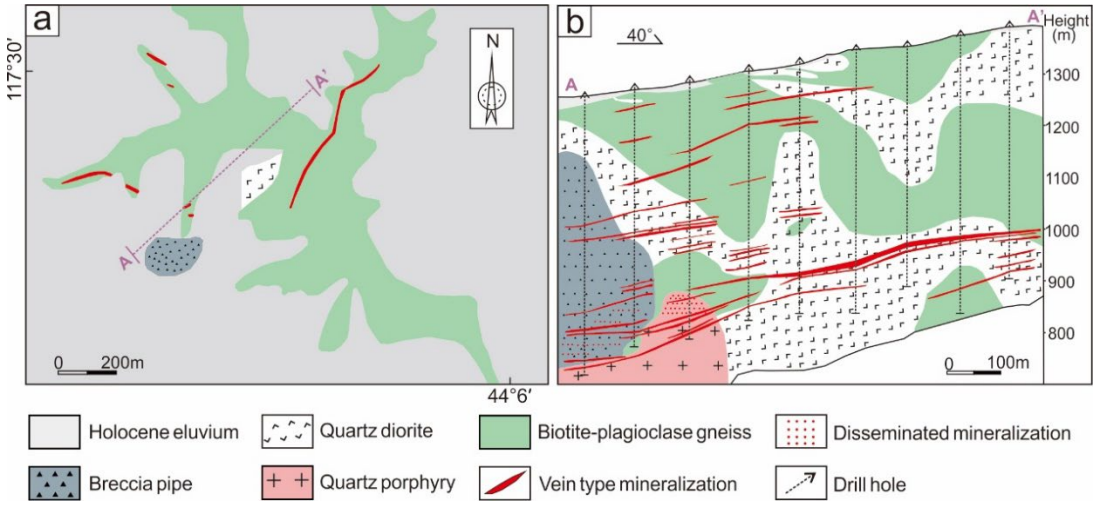

Figure S2. (a) Geological map of the Weilasituo Sn-polymetallic deposit, showing the surface geology and the location of cross-section (Modified after Wang et al., 2017); (b) Cross-section along A-A' exploration line at the Weilasituo Sn-polymetallic deposit, showing the spatial and crosscutting relationships between the parental quartz porphyry intrusion and three types of mineralization, including the vein type Sn-W-Zn-Cu-Mo mineralization, the explosive breccia type Li-Sn-Mo mineralization and the greisenization/disseminated type Sn-Zn-Rb-Nb-Ta mineralization (modified from Liu et al., 2016).

The quartz diorite with a zircon U–Pb age of 308.3 ± 4.2 Ma (Wang et al., 2013) intruded into the Paleoproterozoic Baoyintu Group biotite plagioclase gneiss. It is mainly composed of plagioclase, amphibole, quartz and biotite. The quartz porphyry is a deep concealed intrusion with a light bluish colour as it contains amazonite. This rock is suggested as the ore-genitor rock given its zircon U–Pb age (138 ± 2 Ma; Gao et al., 2019) is consistent with the U–Pb age of cassiterite (138 ± 6 Ma; Wang et al., 2017). The alteration and mineralization are strongest at the upper contact between the quartz porphyry and wall rocks. An explosive breccia pike was developed at the top of the quartz porphyry, and is composed of fragments of biotite plagioclase gneiss and quartz diorite. The cements mainly are quartz and mica, with minor ore minerals occurring locally. Three types of Sn-mineralization can be divided at the Weilasituo Sn-polymetallic deposit, namely quartz vein-type Sn-W-Zn-Cu-Mo mineralization, breccia-type Li-Sn-Mo mineralization and greisen-type disseminated Sn-Zn-Rb-Nb-Ta mineralization. The quartz vein-type mineralization composed of 102 individual veins, and accounts for >80 % Sn at Weilasituo.

As the primary source of tin at Weilasituo, the cassiterite-quartz veins (Fig. S2) are widespread between 900 ~ 1300 m.a.s.l. (meters above sea level), and they occur nearly parallel to each other with a general strike of 25° to 205° and a dip angle of 10° to 20°. These veins often fill open space of tensional cracks and mainly consist of muscovite (Li-rich or locally zinnwaldite), topaz, cassiterite, quartz, fluorite, and a lesser amount of sphalerite, arsenopyrite and wolframite also occur. Muscovite selvages commonly occur at both vein walls whereas ore and other gangue minerals generally appear in vein-centre. Cassiterite can occasionally form aggregated crystals in veins.

In our study, free-grown crystals of quartz-cassiterite veins were collected at 1000 m.a.s.l. where mineral cavities are ubiquitous. Although different samples show slightly different mineral assemblages, their precipitation sequence is rather simple and identical as defined by their paragenesis. In total fourteen cavity samples containing free-standing cassiterite, quartz and/or topaz were obtained from veins with widths ranging from tens to hundreds of centimetres (N17°18′, E117°45′). After detailed characterization, two representative vein-sample containing free-grown cassiterite-quartz crystals were studied for in situ analysis (single fluid inclusion analysis and oxygen isotope study). These two samples were chosen for subsequent detailed studies (Han et al., 2022) because they display clearly-defined mineral paragenesis, which is a requisite to rebuid the fluid evolution history. We also collected a slightly-altered quartz porphyry sample for zircon oxygen isotope analysis (obtaining oxygen isotope composition of primary magmatic fluids).

2. SIMS oxygen isotope analysis

Quartz and cassiterite crystals were analyzed on a CAMECA IMS 1280HR Secondary Ion Mass Spectrometry (SIMS) at the Beijing Research Institute of Uranium Geology (He et al., 2021; Li et al., 2021). Mounts were cleaned by ethanol using an ultrasonic cleaner. Once dried, they were coated with a ~50 nm gold film to improve electrical conductivity. A normal incident electron flood gun was used to compensate for electrical charging. We used ~2 nA Cs^+ ions with an accelerating energy of +10 kV as the primary beam to liberate $^{16}O^-$ and $^{18}O^-$ from the samples. An accelerating voltage for secondary ions was set to –10 kV, so the total bombarding energy was 20 kV. The primary beam was focused in Gaussian mode, and the analytical spot as a square had a size of 15×10 μm^2. An energy window of 60 eV was used at the low energy band, and the mass resolution defined as M/ΔM at 50% peak height was set to 2500.

Prior to analysis, a 20-second sputtering with raster mode was applied to remove the gold coating, and to clean the sample surface. After 60 seconds of automatic beam centering, oxygen isotope measurements were achieved through a 96-second integration, which was divided into 20 cycles, and each cycle contained 4-second isotope measurement plus 0.8-second waiting time. Each spot-measurement took 176 seconds. Oxygen isotopes (^{16}O and ^{18}O) were measured simultaneously on two Faraday cups equipped with 10^{10} and 10^{11} Ω resistors, respectively, and a $^{16}O^-$ intensity of ~3.5×10^9 counts per second (cps) was obtained in our routine measurements.

Measured $^{18}O/^{16}O$ ratios were converted to raw $\delta^{18}O$ values ($\delta^{18}O_{measured}$) through normalizing the measured $^{18}O/^{16}O$ ratios to that of the Vienna Standard Mean Ocean Water (0.0020052, VSMOW) as outlined in Eq. 1,

$$\delta^{18}O_{measured} \text{ in per mil} = (^{18}O/^{16}O_{measured} \div 0.0020052 - 1) \times 1000 . \quad (1)$$

Correction of instrumental mass fractionation was essential to yield true $\delta^{18}O$ values relative to the VSMOW scale. This was achieved through analysing the matrix-matched

reference materials (Qinghu quartz for quartz, and Yongde-Cst for cassiterite) between samples (Li et al., 2022; Tang et al., 2020) following Eq. 2,

$$IMF = \delta^{18}O_{\text{measured value of RM}} - \delta^{18}O_{\text{true value of RM}} \quad . \qquad (2)$$

Once IMF has been obtained, $\delta^{18}O$ values of unknown samples are calculated following Eq. 3,

$$\delta^{18}O_{\text{sample}}\ (\text{VSMOW}) = \delta^{18}O_{\text{measured value of sample}} - IMF \quad . \qquad (3)$$

Instrumental uncertainty from counting statistics for individual analysis (i.e., internal precision) was generally better than 0.2 ‰ (2σ). Accuracy and long-term drift of oxygen isotope analysis were monitored by analysing NBS-28 (for quartz) and BRIUG-Cst (for cassiterite) between samples, and the reproducibility generally was better than 0.3 ‰ (2 SD). All data (magmatic quartz, hydrothermal quartz, and cassiterite) were presented in Table S1 and graphically illustrated in Figure 2.

3. NanoSIMS Al in quartz mapping

Aluminum in quartz was measured on a CAMECA NanoSIMS 50L at the Institute of Geology and Geophysics, Chinese Academy of Sciences. We employed image profile mode analysis (Hao et al., 2016) to further improve the spatial resolution (i.e., ~0.1 μm). In this mode, secondary ion images were acquired by rastering a 50 × 50 μm^2 area with an oxygen beam (~80 pA, Gaussian model) and a beam size of 500 nm in diameter. Four isotopes including ^{7}Li, ^{27}Al, ^{30}Si, and ^{49}Ti were measured with a mass resolution of 10000, and data were acquired for ~4 hours.

Trace element compositions for a given region or profile in the ion images were re-calculated using ImageJ. To avoid degrading the accuracy and precision when measuring Al in quartz at high spatial resolution (i.e., ~0.1 μm), we reported relative Al abundances (i.e., Al/Si) assuming a consistent Si content in quartz at the μm scale, which has no impact on diffusion modelling.

The detection limit is defined as three times of background values, and are ~10 cps for most elements. For SIMS analysis, yield may vary significantly between elements. Hence a higher relative content in cps for a given element does necessarily reflects a higher absolute content in ppm. Al in quartz data for the 9 profiles were presented in Table S2.

4. Oxygen isotope fractionation between mineral and water

Oxygen isotope fractionation between cassiterite/quartz/zircon and water was as follows following our previous study (Li et al., 2022 and references therein),

$$1000 \ln \alpha_{\text{cassiterite-water}} = 2.941\times10^{6}/T^{2} - 11.45\times10^{3}/T + 4.72 \ , \qquad (4)$$

$$1000 \ln \alpha_{\text{quartz-water}} = 4.2\times10^{6}/T^{2} - 3.3\times10^{3}/T \ , \qquad (5)$$

$$1000 \ln \alpha_{\text{zircon-water}} = 1.56\times10^6/T^2 - 3.3\times10^3/T \quad , \qquad (6)$$

where T is the temperature in kelvin.

When using 1000 ln α of mineral-water (i.e., cassiterite-water, quartz-water and zircon water) to derive the oxygen isotope composition of fluids, uncertainties from both oxygen isotope measurements and temperature estimates have been propagated using a Monte Carlo approach (Li et al., 2019).

5. Diffusion modelling

Sharp compositional gradients generated during quartz growth tend to homogenize at high temperatures, in which case elements diffuse out of regions with high contents to surrounding areas with low contents. This diffusion continues as long as the crystal is hosted in hot magmatic-hydrothermal systems, but stops as soon as the crystal cools down. In this regard, the diffusive profile width together with the diffusion speed can be used to estimate the residence time of the crystal in the magmatic-hydrothermal system. The crystal is assumed not to grow or shrink during the diffusion process.

We modeled Al profiles (n=9) as an initial step function modified by diffusional relaxation, hence derived timescales represent maximum values (i.e., when the initial assumption unsatisfied). The growth time for core, mantle and rim of Q1 was donated as t1, t2 and t3, respectively. For core and mantle of Q1, we first modelled their total diffusion time (t1+t2+t3, t2+t3) following the thermal history in Fig. S2A, and then re-calculated their growth time. Timescale and uncertainties from all sources were numerically calculated using the Diffuser software (Wu et al., 2022).

Because the Q1 core has experienced the process of pre-, syn-, and post-mineralization, the diffusion time of pre-mineralization should be calculated after removing the effect of syn- and post-mineralization from Q1 core. Similarly, the diffusion time of syn-mineralization should be calculated after removing the effect of post-mineralization. For example, the modeled parameter *Dt* (*D* is diffusion coefficient and *t* is diffusion time; *Dt* is integral when the diffusion process is not isothermal) in Diffuser (Wu et al., 2022) can be expressed as:

$$\left(\int Ddt\right)_{Q1\,core} = \int_0^{t1} Ddt + \int_0^{t2} Ddt + \left(\int_0^{t3} Ddt\right)_{Q1\,rim} \quad , \qquad (7)$$

$$\left(\int Ddt\right)_{Q1\,mantle} = \int_0^{t2} Ddt + \left(\int_0^{t3} Ddt\right)_{Q1\,rim} \quad , \qquad (8)$$

where t1, t2, and t3 denote the duration of pre-, syn-, and post-mineralization, respectively. The $\left(\int Ddt\right)_{Q1\,core}$, $\left(\int Ddt\right)_{Q1\,mantle}$, and $\left(\int_0^{t3} Ddt\right)_{Q1\,rim}$ can be obtained directly by Diffuser from the measured diffusion profiles. Then, $\int_0^{t1} Ddt$ can be calculated by subtracting $\left(\int Ddt\right)_{Q1\,mantle}$ from$\left(\int Ddt\right)_{Q1\,core}$ and $\int_0^{t2} Ddt$ can be calculated by subtracting

$(\int_0^{t3} Ddt)_{Q1\,rim}$ from $(\int Ddt)_{Q1\,mantle}$. Finally, the duration of t1, t2, and t3 can be calculated by solving the integrals of $\int_0^{t1} Ddt$, $\int_0^{t2} Ddt$, and $\int_0^{t3} Ddt$, respectively.

The Al in quartz data for the 9 profiles were given in Table S2, with a summary of diffusion timescales using diffusivities of Tailby et al. (2018) and Jollands et al. (2020).

References Cited

Gao, X., Zhou, Z., Breiter, K., Ouyang, H., and Liu, J., 2019, Ore-formation mechanism of the Weilasituo tin–polymetallic deposit, NE China: Constraints from bulk-rock and mica chemistry, He–Ar isotopes, and Re–Os dating: Ore Geology Reviews, v. 109, p. 163-183.

Han, L., Pan, J.-Y., Ni, P., and Chen, H., 2022, Cassiterite deposition induced by cooling of a single-phase magmatic fluid: evidence from SEM-CL and fluid inclusion LA-ICP-MS analysis: Geochimica Et Cosmochimica Acta.

Hao, J. L., Yang, W., Luo, Y., Hu, S., Yin, Q. Z., and Lin, Y. T., 2016, NanoSIMS measurements of trace elements at the micron scale interface between zircon and silicate glass: Journal of Analytical Atomic Spectrometry, v. 31, no. 12, p. 2399-2409.

He, S., Li, Y., Wu, L. G., Guo, D. F., Li, Z. Y., and Li, X. H., 2021, High precision zircon SIMS Zr isotope analysis: Journal of Analytical Atomic Spectrometry, v. 36, no. 10, p. 2063-2073.

Jollands, M. C., Bloch, E., and Müntener, O., 2020, New Ti-in-quartz diffusivities reconcile natural Ti zoning with time scales and temperatures of upper crustal magma reservoirs: Geology, v. 48, no. 7, p. 654-657.

Li, Y., Zhang, S., Hobbs, R., Caiado, C., Sproson, A. D., Selby, D., and Rooney, A. D., 2019, Monte Carlo sampling for error propagation in linear regression and applications in isochron geochronology: Science Bulletin, v. 64, no. 3, p. 189-197.

Li, Y., Tang, G. Q., Liu, Y., He, S., Chen, B., Li, Q. L., and Li, X. H., 2021, Revisiting apatite SIMS oxygen isotope analysis and Qinghu-AP reference material: Chemical Geology, v. 582.

Li, Y., He, S., Zhang, R.-Q., Bi, X.-W., Feng, L.-J., Tang, G.-Q., Wang, W.-Z., Huang, F., and Li, X.-H., 2022, Cassiterite oxygen isotopes in magmatic-hydrothermal systems: in situ microanalysis, fractionation factor, and applications: Mineralium Deposita, v. 57, no. 4, p. 643-661.

Liu, Y., Jiang, S., and Bagas, L., 2016, The genesis of metal zonation in the Weilasituo and Bairendaba Ag–Zn–Pb–Cu–(Sn–W) deposits in the shallow part of a porphyry Sn–W–Rb system, Inner Mongolia, China: Ore Geology Reviews, v. 75, p. 150-173.

Mao, J. W., Ouyang, H. G., Song, S. W., Santosh, M., Yuan, S. D., Zhou, Z. H., Zheng, W., Liu, H., Liu, P., Cheng, Y. B., and Chen, M. H., 2020, Geology and metallogeny of tungsten and tin deposits in China: SEG Spec Pub, v. 22, p. 411-482.

Tailby, N. D., Cherniak, D. J., and Watson, E. B., 2018, Al diffusion in quartz: American Mineralogist, v. 103, no. 6, p. 839-847.

Tang, G. Q., Liu, Y., Li, Q. L., Feng, L. J., Wei, G. J., Su, W., Li, Y., Ren, G. H., and Li, X. H., 2020, New Natural and Fused Quartz Reference Materials for Oxygen Isotope Microanalysis: Atomic Spectroscopy, v. 41, no. 5, p. 188-193.

Wang, F., Bagas, L., Jiang, S., and Liu, Y., 2017, Geological, geochemical, and geochronological characteristics of Weilasituo Sn-polymetal deposit, Inner Mongolia, China: Ore Geology Reviews, v. 80, p. 1206-1229.

Wang, X.-y., HOU, Q.-y., Wang, J., CHEN, Y.-l., LIU, J.-b., WANG, Z., and LI, D.-p., 2013, SHRIMP geochronology and Hf isotope of zircons from granitoids of the Weilasituo deposit in Inner Mongolia: Geoscience, v. 27, no. 1, p. 67.

Wu, L. G., Li, Y., Jollands, M. C., Vermeesch, P., and Li, X. H., 2022, Diffuser: A user-friendly program for diffusion chronometry with robust uncertainty estimation: Computers & Geosciences, v. 163.